Journal of Applied Physics

RESEARCH ARTICLE | FEBRUARY 27 2023

Study on the plasma characteristics in a needle-plate dielectric barrier discharge with a rotating dielectric plate

Guanglin Yu ; Nan Jiang ; Bangfa Peng ; Haoyang Sun ; Zhengyan Liu ; Jie Li

J. Appl. Phys. 133, 083302 (2023)
https://doi.org/10.1063/5.0136280

AIP Publishing

Journal of Applied Physics | ARTICLE | scitation.org/journal/jap

Study on the plasma characteristics in a needle-plate dielectric barrier discharge with a rotating dielectric plate

Cite as: J. Appl. Phys. 133, 083302 (2023); doi: 10.1063/5.0136280
Submitted: 24 November 2022 · Accepted: 2 February 2023 ·
Published Online: 27 February 2023

View Online | Export Citation | CrossMark

Guanglin Yu,[1] Nan Jiang,[1] Bangfa Peng,[1] Haoyang Sun,[2] Zhengyan Liu,[2] and Jie Li[1,a)]

AFFILIATIONS

[1]School of Electrical Engineering, Dalian University of Technology, Dalian 116024, China
[2]School of Environmental Science and Technology, Dalian University of Technology, Dalian 116024, China

[a)]**Author to whom correspondence should be addressed:** lijie@dlut.edu.cn

ABSTRACT

The enhancement of plasma generation in atmospheric pressure dielectric barrier discharge (DBD) is gaining increasing interest for various plasma applications. In this paper, the effect of surface charges moving with the rotating dielectric plate on improving the generation of streamer channels is investigated by a statistical analysis of electrical measurements, optical diagnostics, and numerical simulation in a needle-plate DBD device with a rotating dielectric plate. Results suggest that rotating the dielectric plate can improve the spatiotemporal distribution of streamer channels by inducing a bending of the streamer channels and an increase in the number of discharges. Statistical results show that the number of current pulse and discharge energy are increased by 20% and 47%, respectively, at the rotating speed of 160 rps (revolution per second). Based on the interaction between the applied electric field and the electric field induced by surface charges, a formula is proposed to govern the effect of rotating the dielectric plate on the discharge energy and streamer bending. To further understand the mechanism of the influence of rotating the dielectric plate on plasma properties, a 2D fluid model is implemented, and the reduced electric field and streamer propagation are analyzed. Results show that the effective transfer and reuse of surface charges play an important role in the enhancement of plasma generation.

I. INTRODUCTION

Dielectric barrier discharge (DBD), as an important non-thermal plasma source, has been used for various applications, such as ozone generation, pollutant degradation, biomedicine, energy conversion, and material surface modification.[1–8] Generally, the DBD plasma presents a filamentary regime with numerous streamer channels at atmospheric pressure attributed to the high *pd* value.[9,10] Many studies have shown that it is beneficial for enhancing the energy efficiency concerning plasma applications to improve plasma generation.[11–13] The plasma characteristics are dependent on various factors, including reactor configuration, power supply parameters, and gas environments. The reduction in the gas gap and the enhancement of the applied voltage can result in the improvement of the number and spatial distribution of microdischarges.[14,15] However, too small air gap and too high voltage may result in the breakdown of dielectric materials.[15,16] In addition, increasing the frequency of the power supply and the adoption of the dual AC/RF excitation can enhance the plasma generation;[17–19] however, high frequencies may lead to a reduction in the energy efficiency in some plasma applications such as pollutant degradation and ozone generation.[15,20] Therefore, it is important for DBD applications to achieve an increase in plasma generation without upgrading voltage and frequency levels.

Surface charges play an important role in DBD, and many studies have shown that the modulation of the surface charge distribution is an effective method to enhance plasma generation.[21–24] Somekawa *et al.* suggest that the clearance of memory effects for surface charges by a voltage of opposite polarity can improve the discharge uniformity.[23] Choi *et al.* found that surface charges spreading on the dielectric surface can enhance the spatial distribution of discharges by increasing the surface conductivity of a dielectric plate.[24] The above studies focus on the effect of the memory effect of surface charges on the spatiotemporal distribution for different discharge cycles. However, relatively few studies have been conducted to improve plasma generation in the same discharge cycle by optimizing the distribution of surface charges. The electric field induced by surface charges is opposite to that of the applied voltage, which is not conducive to the generation of discharges at the same position during the same discharge cycle.[25,26] Beyond that, surface charges can also suppress the formation of streamer channels at the surrounding positions,[21,27] which further limits the spatiotemporal expansion of streamer channels. For AC-driven DBD, the effective transfer of surface charges during the rise of the applied voltage can weaken the electric field induced by surface charges, indicating that the total electric field (the electric field of an applied voltage minus that induced by surface charges) in the gas gap can be enhanced. Therefore, achieving an efficient transfer of surface charges is advantageous for the generation of subsequent streamer channels at the same discharge period. Furthermore, these surface charges are expected to be efficiently utilized in subsequent discharge cycles. Considering the fact that surface charges are trapped by the traps on the dielectric surface,[2,28] these surface charges can travel with a rotating dielectric plate. Hence, we propose to enhance plasma generation via effective transfer and reuse of surface charges in a rotating dielectric plate DBD without upgrading the voltage and frequency levels. The plasma generation in a single pin-plate DBD offers the advantage of easy diagnosis, and the influence mechanism of a rotating dielectric plate on the plasma characteristics in this type DBD is the same as that in the multi-pin-plate and multi-pin-cylinder DBDs commonly used in plasma applications, such as plasma agriculture[29] and pollutant degradation.[30] Therefore, a single needle-plate DBD is employed to study the physical mechanism of enhanced plasma generation by a rotating dielectric plate.

In this work, the plasma generation in a needle-plate DBD device with a rotating dielectric plate is investigated. The discharge images of different exposure times are taken by a digital camera and an intensified charge-coupled device (ICCD) camera to investigate the effect of the rotating dielectric plate on the spatiotemporal expansion of streamer channels. The statistical studies of electrical measurements are implemented to study the influence of the rotating dielectric plate on the discharge energy and the amplitude and number of current pulses. Based on the matching principle of the rotating speed and applied voltage frequency, the formula that determines whether the discharge power can be enhanced is proposed. The mechanism of the rotating dielectric plate on plasma generation is analyzed based on a 2D fluid simulation model. The enhanced plasma generation by rotating a dielectric plate is demonstrated in a single pin-plate DBD without upgrading voltage and frequency levels, which can provide the theoretical and experimental foundation for this method to be generalized to the plasma applications based on the multi-pin-plate and multi-pin-cylinder DBDs.

II. EXPERIMENTAL SETUP AND NUMERICAL APPROACH

A. Experimental setup

The needle-plate DBD experimental setup with a rotating dielectric plate is built and shown in Fig. 1(a). The setup is composed of a tungsten needle electrode and a grounded dielectric plate connected to a spindle motor through an acrylic stand. The dielectric is a circular quartz glass with a thickness of 1 mm and a diameter of 70 mm. A 0.1 mm thick copper foil is adhered on the surface of the quartz glass and fixed on the acrylic stand. The copper foil extending on the side of the dielectric plate is connected to the ground through a carbon fiber brush to ensure the stability of the circuit during the rotation of the dielectric plate. The horizontal distance between the needle tip and the central axis of the ground electrode is 20 mm and the gas gap is 3 mm. The rotational speed of the dielectric plate is adjustable from 0 to 180 rps (revolutions per second). The reactor is driven by an AC power source connected to a transformer. The voltage and current waveforms are detected by a high-voltage probe (Tektronix P6015A) and a Pearson current coil (Model 6595) and recorded by a digital phosphor oscilloscope (RIGOL MSO5104, 100 MHz and 8.0 Gs/s). Charge–voltage diagrams are derived by an additional serial capacitance (100 nF) and used to calculate the discharge power.[31] To study the streamer morphology characteristics, the discharge images are taken by a digital camera (Canon EOS 80D) and an ICCD camera (Princeton, PI-MAX 3 1024i) that can be triggered via a signal delivered from the digital phosphor oscilloscope. To collect the optical emission spectra (OES), the light emitted from the discharge is focused by a lens into a fiber connected to the entrance slit (width: 1.3 mm) of a spectrometer (Princeton, Action SP2750) with an ICCD array.

B. Numerical approach

The 2D PArallel Streamer Solver with KinEtics (PASSKEy) code is adopted to study the effect of the rotating dielectric plate on streamer propagation. Code feasibility verification, detailed descriptions for mathematical formulations, and numerical approaches can be found in literatures.[32–34] The 2D fluid code based on the local mean energy approximation (LMEA) approach is adopted. The mobility and diffusion coefficients for electron and electron energy and the reaction rate coefficients can be calculated based on LMEA.[34] The DBD in air is described using coupled continuity equations with drift-diffusion approximation, Helmholtz equations for photoionization, the energy conservation equation for mean electron energy, and Poisson's equation for the electric field. Detailed descriptions are given in the supplementary material.

A volume fraction of 0.79 N_2 and 0.21 O_2 is adopted for air composition. The gas pressure and temperature are set to 1 atm and 293.15 K. Eighteen species including neutral, charged, and excited species and 62 reactions are adopted in the kinetic reactions model, and detailed kinetic reactions are shown in Table S1 in the supplementary material. A total computational domain of $10 \times 7\ \mathrm{mm}^2$ is shown in Fig. 1(b). The curvature radius of the tungsten needle at the tip is $50\,\mu$m in our experiment; therefore, the expression of the needle electrode is assumed to be $y \geq 10000 \times (x - x_0)^2 + y_0$ (unit: m), where x_0 and y_0 correspond to the abscissa and ordinate at the needle tip and are set to 5×10^{-3} and 4×10^{-3} m, respectively. The minimum cell size of $4\,\mu$m is implemented and the computational domain contains 219 716 plasma nodes. In the fact of such a complex physical module, the numerical calculation for an entire voltage cycle

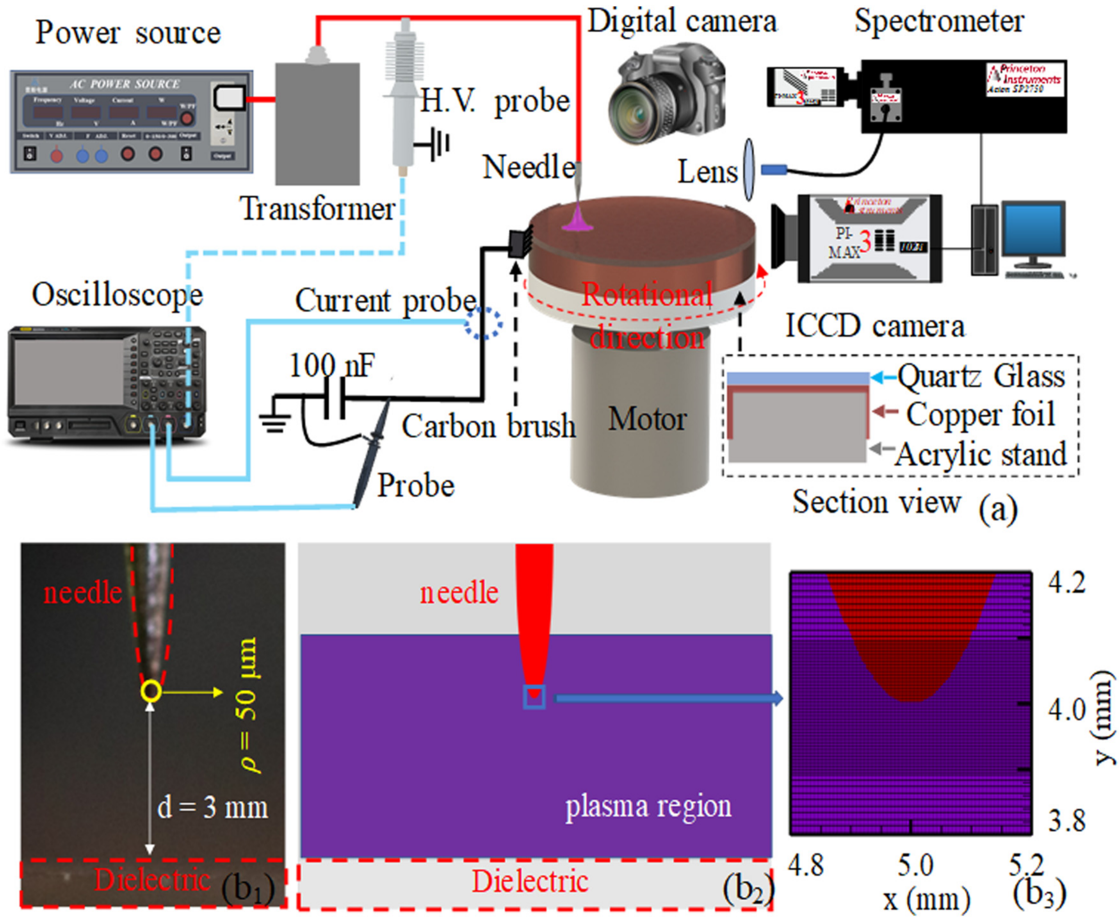

FIG. 1. (a) Experimental system diagram of the rotational dielectric plate DBD. (b) The computational domain in numerical simulation. (b_1) Geometric configuration of the needle-plate DBD. (b_2) Schematic of the computational domain. (b_3) Mesh distribution around the needle tip.

greatly increases the computational cost for the frequency of 400 Hz. Taking account of the fact that this paper only focuses on the influence of positional changes for surface charges on the streamer development, the single streamer generation and development under the peak voltage instead of the AC waveform is adopted and the similar method is adopted in papers.[35,36]

III. RESULTS AND DISCUSSION

A. Effect of the rotating dielectric plate on electrical and optical characteristics of plasma

To study the effect of rotating the dielectric plate on plasma characteristics, the discharge powers at different rotational speeds for 400 Hz and 10 kV are shown in Fig. 2(a), where each power is the average value of 10 groups of measurements. It can be found that the discharge power can be improved under appropriate rotating speeds. For example, compared with 0 rps (0.45 W), the discharge power is increased by 47% at the rotational speed of 160 rps (0.66 W). However, there is no obvious regularity in the variation of discharge power as the rotational speed increases from 0 to 180 rps. Moreover, it can be found that the discharge powers in the rotating dielectric plate DBD are lower than that in the stationary electrode DBD at some rotational speeds. For example, the discharge power reaches the local minimums (0.32 W for 100 rps and 0.24 W for 130 rps), which are lower than that (0.45 W) for the stationary electrode, as shown in Fig. 2. The above results indicate that rotating the dielectric plate can enhance the discharge energy only at some specific speeds, and the corresponding theoretical mechanism will be analyzed in Sec. III B. In addition, it is significant to study the effective capacitance in DBD to gain a deeper understanding of the influence of rotating the dielectric plate on plasma characteristics. The Lissajous graphs for three typical rotating speeds (stationary electrode: 0 rps, power suppressed: 130 rps, and power enhanced: 160 rps) are shown in Fig. 2(b), where k_n represents the cell capacitance without discharge (the dielectric capacitance and gap capacitance in series) and k_d stands for the

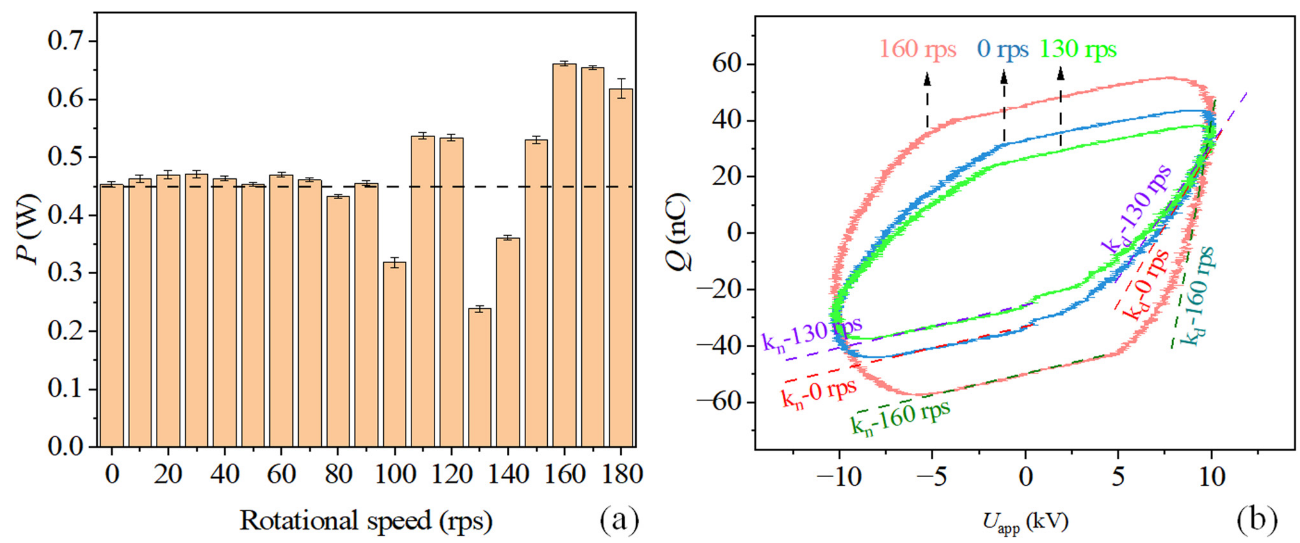

FIG. 2. (a) Discharge powers at different rotational speeds for 400 Hz and 10 kV. (b) The *QV* diagram at the rotating speeds of 0, 130, and 160 rps.

measured capacitance, which is referred to as effective dielectric capacitance and depends on the surface charge area.[37,38] It can be found that k_n is equal in three cases, indicating that rotating the dielectric plate does not change the cell capacitance. Also, k_d-0 rps is greater than k_d-130 rps and less than k_d-160 rps, indicating that rotating the dielectric plate can affect the dielectric area covered by surface charges. Then, for the case of increased discharge, more regions on the dielectric plate are covered by surface charges.

Studying the appearance of the streamer is a key point for gaining insight into plasma properties. The long-term morphological characteristics of the streamer channels are studied by using a digital camera with an exposure time of 250 ms (100 voltage cycles). The streamer images in an anodic needle half-cycle are obtained using an ICCD camera (exposure time: 1.25 ms, gain: 30). The results are displayed in Fig. 3, where the speeds greater than or equal to 62 rps are obtained based on the interaction between the applied electric field and the electric field induced by surface charges, which will be mentioned in Sec. III B. By comparing those images, it can be found that for stationary electrodes, the streamer channel is vertical [Fig. 3(a)]. For speeds from 20 to 73 rps, the streamer channels bend to the right direction, which is consistent with the direction of the tangential direction of the dielectric plate rotation. However, an interesting phenomenon can be found that the direction of streamer bending does not always coincide with that of the rotating dielectric plate. For 80, 100, and 133 rps, the streamers bend to the right direction, as shown in Figs. 3(g), 3(i), and 3(k). For 89, 114, and 160 rps, the discharges bend to the left direction, which is opposite to the rotating direction, as shown in Figs. 3(h), 3(j), and 3(l). For the latter case, rotating the dielectric plate can lead to higher light intensity, more streamer branches, and wider spatial distribution of streamers. The above results show that the effect of different rotational speeds on the streamer channel is different, and only rotating the dielectric plate at proper rotational speeds can enhance the distribution of streamer channels.

According to the results in Fig. 3, three typical rotational speeds (0 rps for stationary dielectric plate, 62 rps for low speed, and 160 rps for high speed) are selected to further study the streamer morphologies at different times in an applied voltage cycle. Figures $4(a_1)$–$4(a_3)$ give the waveforms of single-shot voltage and current and six time periods of capturing ICCD images. Moreover, for the stationary electrode, the magnified current waveform in the cathodic needle half-cycle is recorded after increasing the resolution of time and amplitude in the oscilloscope and shown in Fig. $4(a_{1m})$. Δt_1 (−175–25 μs) is near zero voltage, and Δt_2 (25–225 μs), Δt_3 (225–425 μs), and Δt_4 (425–625 μs) are at the rising edge of the applied voltage on an anodic needle half-cycle. Δt_5 (625–825 μs) is at the falling edge on the anodic needle half-cycle. Δt_6 (1250–1875 μs) is at the rising edge on the cathodic needle half-cycle. The images corresponding to those periods are presented in Figs. 4(b)–4(d). Results show that the streamer channels can be found in Δt_1–Δt_4 [Figs. $4(b_1)$–$4(b_4)$] for 0 rps. Although there are some streamer branches near the dielectric, the streamer channel is basically vertical. The applied voltages corresponding to Δt_1 is close to 0 kV, indicating that the discharge in Fig. $4(b_1)$ is dominated by residual surface charges.[27,39] Moreover, the surface discharge induced by the volume discharge can be found on the dielectric surface, and the propagation distance is about 3.2 mm [Fig. $4(b_4)$]. At the falling edge of the voltage, the streamer cannot be ignited except for the discharge near the zero voltage, which is because that the surface charges accumulated on the dielectric will inhibit the discharge on the same voltage cycle.[27,39] Then, the current pulse and the streamer channel corresponding to Δt_5 are not found in Figs. $4(a_1)$ and $4(b_5)$. The corona discharge is found in the cathodic needle half-cycle (Δt_7), as shown in Fig. $4(b_6)$, which corresponds to the lower amplitude

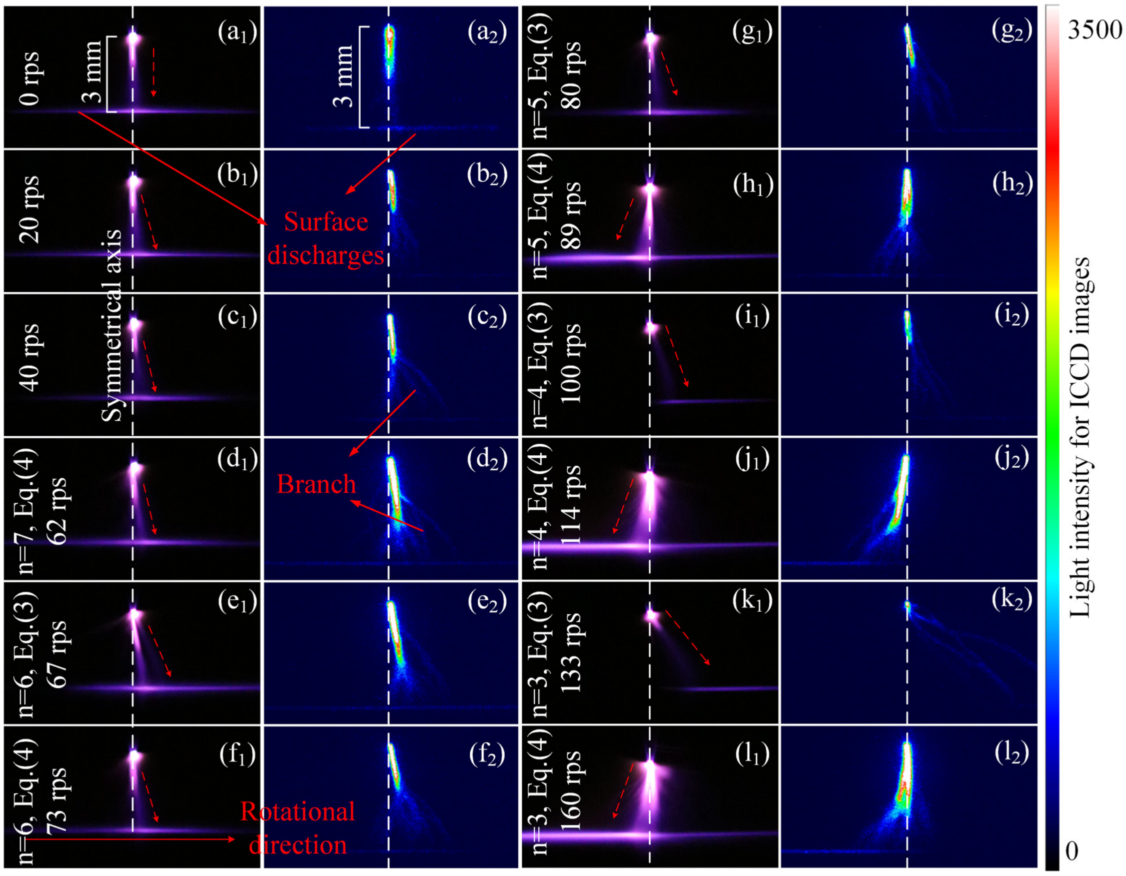

FIG. 3. Discharge images at different rotational speeds at 400 Hz and 10 kV. (a_1)–(l_1) Images with the exposure time of 250 ms. (a_2)–(l_2) Images with the exposure time of 1.25 ms in the anodic needle half-cycle. n corresponds to that in Eqs. (3) and (4) and will be mentioned in Sec. III B.

current pulse in Fig. $4(a_{1m})$. This phenomenon of finding different discharges in the positive and negative periods is due to the fact that negative discharges require much higher ignition voltages.[40–42] For 62 rps, streamer channels can also be observed in Δt_1–Δt_4 [Figs. $4(c_1)$–$4(c_4)$], and the corona discharge is shown in t_6 [Fig. $4(c_6)$], which is consistent with that for 0 rps. Moreover, all the streamer channels at 62 rps bend to the right, which is consistent with that in Fig. 3(d). For 160 rps, the corona discharge rather than the streamer discharge is observed in Δt_1, as shown in Fig. $4(c_1)$. However, the current pulse and the streamer channel corresponding to the falling edge of the voltage (Δt_5) can be found in Figs. $4(a_3)$ and $4(d_5)$. The streamer channels at 160 rps bend to the right, which is consistent with that in Fig. 3(l). It can be indicated that rotating the dielectric plate not only enhances the spatial distribution of the streamer, but also influences the time phase of the discharge.

The number and amplitude of current pulses are positively correlated with the number and intensity of discharges, respectively, in a pin-plate DBD. Then, the investigation of the effect of rotating the dielectric plate on current pulse parameters is beneficial for gaining insight into the enhancement mechanism of plasma generation. Current–voltage waveforms are recorded at 0 and 160 rps to investigate the effect of rotating the dielectric plate on the current pulse under increased discharge power. The results are shown in Fig. 5(a), where the current waveform is accumulated 130 times. It is worth noting that the electromagnetic interference generated by the motor may affect the statistics of corona discharges, while it does not influence the statistics of streamer discharges, as shown in Fig. S1 in the supplementary material. Therefore, this work presents only the statistical results of the discharges in the positive half-cycle. The time probability distribution map of the current pulse is shown in Fig. 5(b), which is obtained according to the statistical analysis of the current signal of 130 times (260 voltage cycles in total) in Fig. 5(a). It can be found that the discharge can be ignited before the start of the anodic needle half-cycle for a stationary electrode and the current pulse disappears after the applied voltage reaching peak [Fig. 5(b)], which is consistent with the result in Fig. $4(a_1)$. For 160 rps, the current pulse appears after the start of the anodic needle half-cycle; however, the corresponding probability is much lower than that of the stationary electrode, as shown in Figs. $5(b_1)$ and $5(b_2)$.

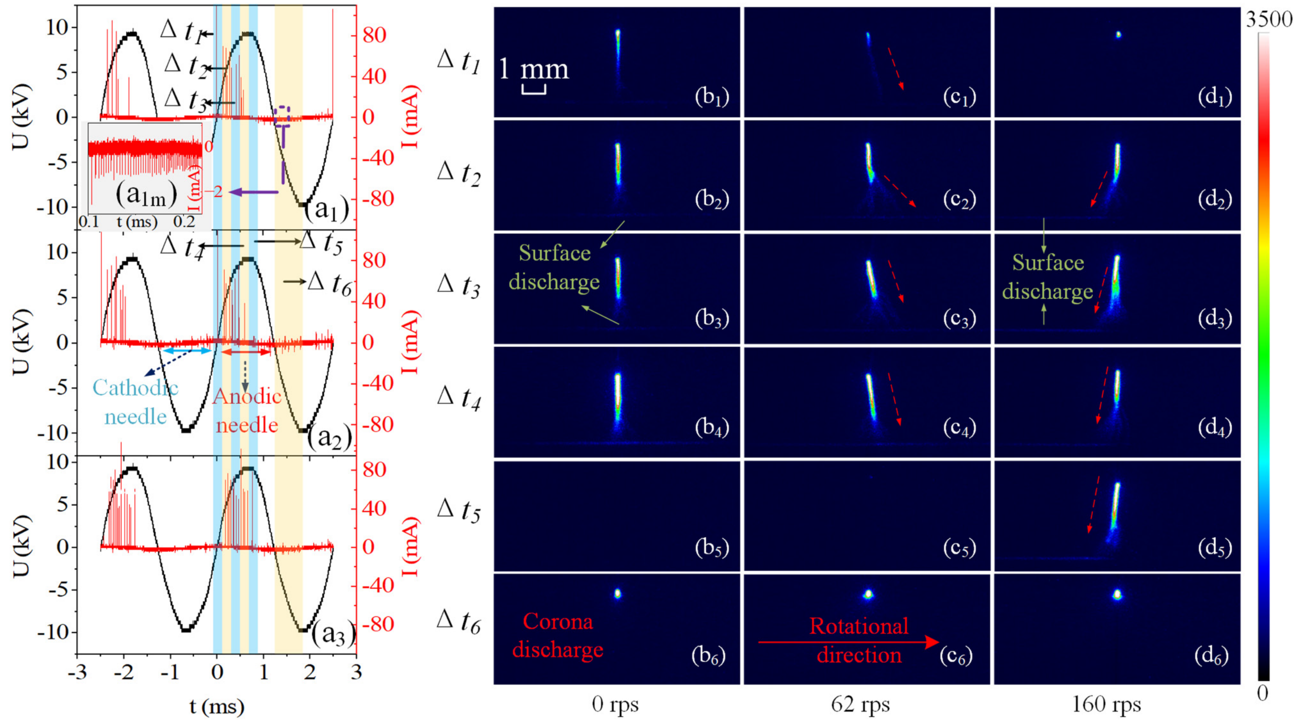

FIG. 4. (a_1)–(a_3) Single-shot voltage and current waveforms at 0, 62, and 160 rps. (a_{1m}) The magnified current waveform in the cathodic needle half-cycle. (b)–(d) Discharge images taken by the ICCD camera. Where $\Delta t_1 = \Delta t_2 = \Delta t_3 = \Delta t_4 = \Delta t_5 = 200\,\mu$s and $\Delta t_6 = 625\,\mu$s.

In addition, the discharge can be ignited even after the voltage peaks [Fig. 5(b_2)], which is consistent with Figs. 4(a_3) and 4(d_5).

The average amplitude and number of pulses for 260 voltage cycles of current pulses in Fig. 5(a) are statistically analyzed, and the result is presented in Fig. 6(a). It can be seen that for 0 rps, the average amplitude and the number of current pulses are 56 mA and 10, respectively. For 160 rps, the average amplitude and the number of current pulses are 61 mA and 12, respectively. Then, compared to the stationary electrode DBD, the amplitude and number of current pulses are increased by 8.9% and 20% at 160 rps. In addition, the probability distribution map of the current pulse amplitude is shown in Fig. 6(b). It can be found that the maximum probability appears at 55 and 68 mA for 0 and 160 rps, which indicates that the amplitude with the highest probability for rotating the dielectric plate is higher than that of the stationary electrode. Therefore, the improvement in the discharge power is due to the increase in the number and amplitude of the current pulses.

To further investigate the effect of rotating the dielectric plate on plasma properties, the OES in the range of 300–420 nm for 0, 62, and 160 rps are measured and shown in Fig. 7(a). The OES are mainly composed of the second positive bands of N_2 ($C^3\Pi_u \rightarrow B^3\Pi_g$) and the first negative bands of N_2^+ ($B_2\Sigma_u^+ \rightarrow X_2\Sigma_g^+$).[43,44] The light intensities at 337 nm for different speeds are shown in Fig. 7(b). The rotating dielectric plate can increase the intensity of the spectrum, which corresponds to the increase in discharge power (Fig. 2). The intensity ratio of the FNS(0, 0) and SPS(2, 5) for nitrogen bands (I_{391}/I_{394}) can be used to represent the reduced electric field (E/N) in atmospheric pressure discharge.[30,45–47] The effect of rotating the dielectric plate on I_{391}/I_{394} under different speeds is shown in Fig. 7(b). It can be seen that the rotating dielectric plate can enhance the ratio of I_{391}/I_{394}, which indicates that higher E/N can be obtained in the rotating dielectric plate DBD.

B. Matching mechanism of the rotating speed and the frequency of the applied voltage

The movement of the dielectric plate is the key to enhance the discharge energy and the spatial and temporal distribution of the streamer channel. Considering the fact that surface charges are trapped by the traps on the dielectric surface,[2,28] these surface charges can travel with the moving dielectric plate at the same speed, which will be demonstrated in Sec. III C. Then, the mechanism schematic diagram of surface charges affecting subsequent discharge is shown in Fig. 8, where the red stands for positive charges and the blue represents negative charges. A simple case in which surface charges can inhibit the discharge is presented in Fig. 8(a). Assuming only once electrical breakdown per half-cycle of the voltage, the surface charges accumulate on the dielectric

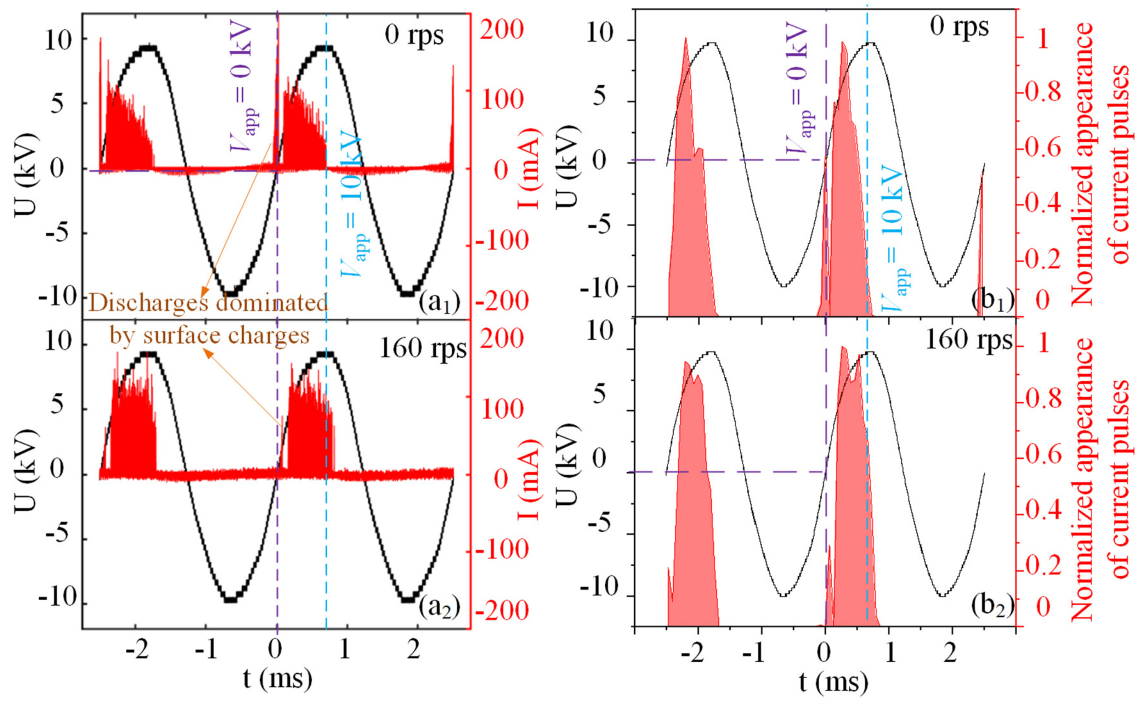

FIG. 5. (a) Current–voltage waveform of the discharge with the rotational speeds of 0 and 160 rps, where current waveform is accumulated 130 cycles. (b) Time probability distribution map of current pulses.

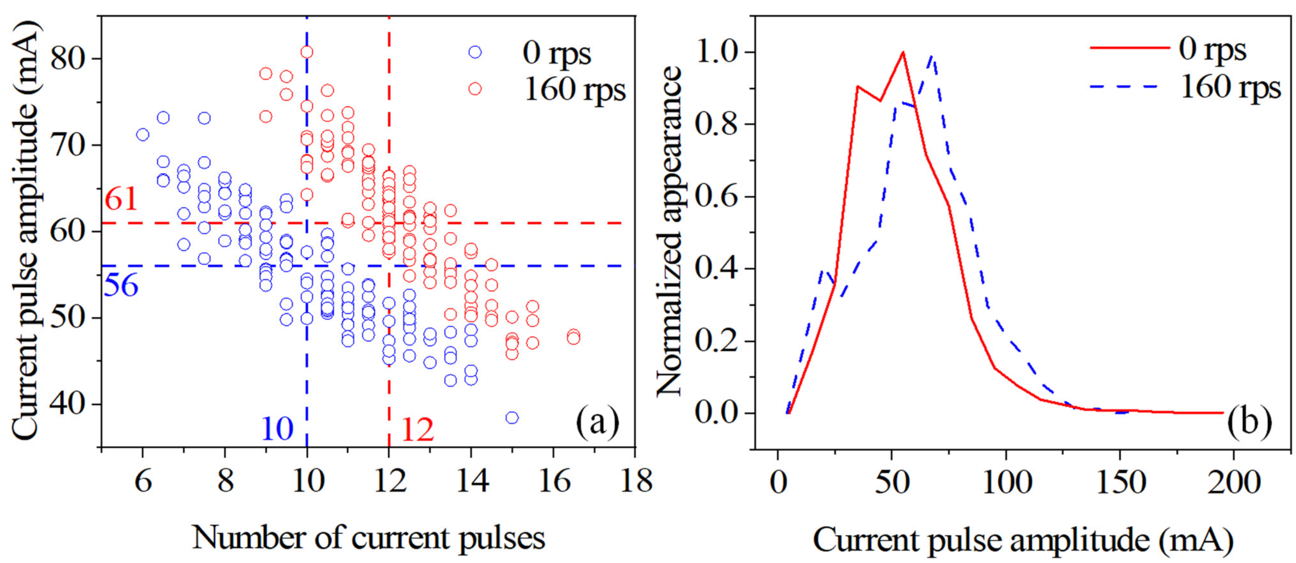

FIG. 6. (a) The correlation diagram between the average amplitude and the number for current pulses and (b) probability distribution map of current pulse amplitude histograms.

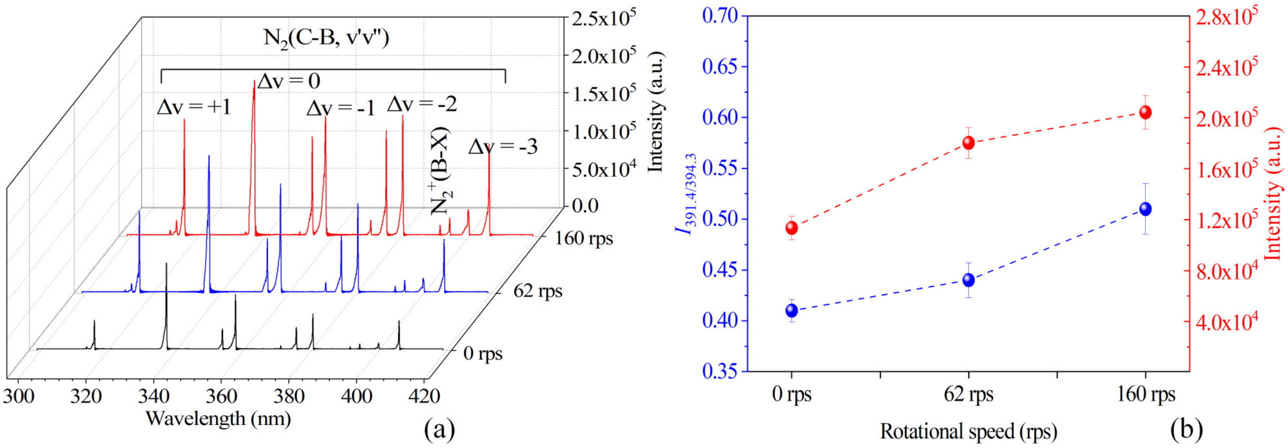

FIG. 7. (a) Optical emission spectrum in the wavelength range of 300–420 nm for different rotating speeds. (b) The intensity of $I_{391.4}/I_{394.3}$ and the light intensity at 337 nm for different speeds.

twice during the dielectric plate making one revolution when the cycle of the rotating dielectric plate and the voltage cycle are the same. Figure 8(a_1) shows the distribution of surface charges after the discharge in a positive half-cycle. Before the next negative half-cycle discharge, the negative surface charges are just below the needle electrode due to dielectric rotation [Fig. 8(a_2)]. In this case, the direction of the electric field induced by surface charges is opposite to that of the applied electric field, and the discharge is inhibited. In the other case, when the voltage cycle is 1.5 times the rotation cycle of the dielectric plate, the surface charges are accumulated three times on the dielectric surface during the dielectric plate rotating once. The surface charges distribution after the discharge in a positive half-cycle is presented in Fig. 8(b_1). Before the next negative half-cycle discharge, the positive surface charges are just below the needle electrode [Fig. 8(b_2)]. The electric field induced by the surface charge is directed in the same direction as the applied voltage and, thus, promotes the discharge. In this case, the surface charges that re-enter the discharge area can be reused effectively by subsequent reverse discharges.

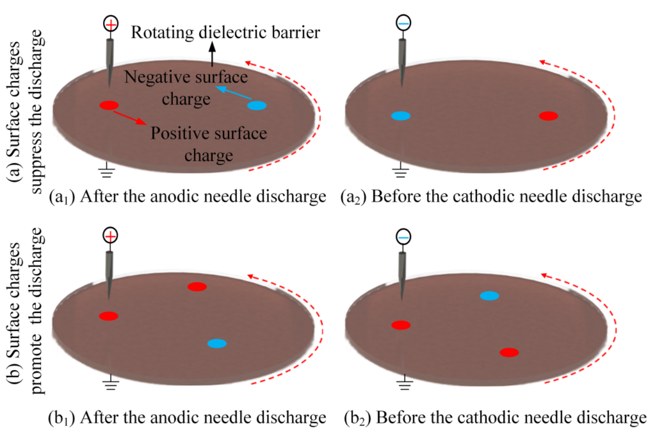

FIG. 8. Schematic diagram of the surface charges affecting subsequent discharge. (a) Surface charges suppress subsequent discharge. (b) Surface charges enhance subsequent discharge.

In general, the voltage cycle is smaller than the rotation cycle and the surface charges accumulated in different voltage cycles can exist on a dielectric surface simultaneously. Therefore, the matching principle can be generalized as follows. If the electric field induced by the surface charge moving with the dielectric is opposite to that of the applied voltage before the start of each discharge, the discharge is suppressed. In this case, an even number of surface charges are accumulated when the electrode rotates once, which can be described via

$$T_a = \frac{T}{n}. \tag{1}$$

On the other hand, if the electric field induced by the surface charge moving with the dielectric is the same as that of the applied voltage before the start of each discharge, the discharge can be promoted. In the case, an odd number of surface charges are accumulated when the dielectric plate rotates once, which can be described via

$$T_a = \frac{T}{n - 0.5}, \tag{2}$$

where T_a denotes the applied voltage cycle, T is the rotation period of the dielectric plate, and n is the positive integer.

To correspond to experimental conditions, Eq. (1) can be recast as follows by replacing T_a with $\frac{1}{f_a}$, T with $\frac{1}{\omega}$:

$$\omega = \frac{f_a}{n}. \tag{3}$$

Equation (2) can be recast as follows by the same method,

$$\omega = \frac{f_a}{n - 0.5}, \tag{4}$$

where f_a is the voltage frequency (unit: Hz) and ω denotes the rotational speed of the dielectric plate (unit: rps).

Based on the above matching principle, the effect of matching between the dielectric plate rotation speed and the applied voltage frequency on the discharge power is shown in Table I. The numbers in the schematic diagram of the surface charge distribution represent the surface charges accumulated at different discharge cycles. It can be found that for 400 Hz, the discharge could be suppressed when the rotational speeds are 100 and 133 rps, and the discharge can be promoted when the rotational speeds are 110 and 160 rps, which is consistent with experimental results in Fig. 2. The results indicate that the irregular variation in power in Fig. 2 is attributed to surface charges moving with the dielectric plate.

To further confirm the above matching principle, Table I shows the matching results of rotational speeds and frequencies when the frequencies are 200 and 100 Hz. The corresponding powers are measured at the peak voltage of 10 kV and shown in Fig. 9. It can be found that for 200 Hz, the discharge is suppressed at 100 and 66 rps, and the discharge can be promoted at 133 and 80 rps in Table I. The experimental results show that the smaller discharge powers are found at 100 and 70 rps, and the higher powers appear at 130 and 80 rps for 200 Hz, which is consistent with the matching principle in Table I. Also, Fig. 9 shows that the smaller discharge powers are at 100 and 50 rps, and the higher discharge power is at 70 rps for 100 Hz, which is also consistent with the matching results in Table I. Then, the interaction between the applied electric field and the electric field induced by surface charges plays an important role in the discharge power in the DBD and Eqs. (3) and (4) can determine whether the discharge power can be enhanced.

C. Verification of surface charges moving with the rotating dielectric plate

The movement of the surface charges with the dielectric plate is considered to be responsible for the above experimental results. Then, it is necessary to validate the movement of surface charges with the rotating dielectric plate. In general, the measurement techniques based on the electrostatic probe and the Pockels electro-optic effect are used to study the distribution of surface charge.[48–50] However, these methods are difficult to be achieved in our experiments due to that the former is affected by the original electric field and the latter is limited by the structure of the rotating dielectric plate. Here, we propose the introduction of a second ground electrode to confirm that the surface charge can move with the dielectric plate. The diagram of the experimental setup is presented in Fig. 10(a). The second ground electrode is at the symmetrical position of the high-voltage electrode about the axis of the dielectric plate and the gas gap is set to 1 mm. If the surface charges can move with the dielectric and pass under the second ground electrode, the electric field of the surface charges could induce discharge. Discharge images with exposure times of 250 ms at

TABLE I. The effect of matching between the rotating speed and the applied voltage frequency on the discharge. T and ω denote the period and angular velocity of the rotating electrode.

f (Hz)	Surface charge distribution / Rotational speed	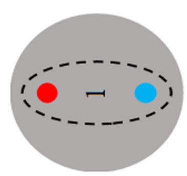	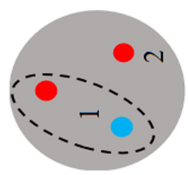	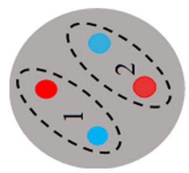	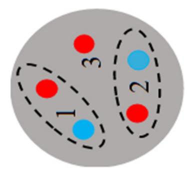	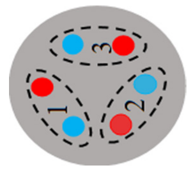	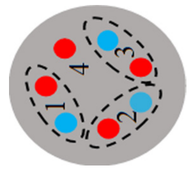	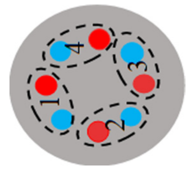	⋮
100	T (ms)	10	15	20	25	30	35	40	⋮
	ω (rps)	100	67	50	40	33	29	25	⋮
200	T (ms)	5	7.5	10	12.5	15	17.5	20	⋮
	ω (rps)	200	133	100	80	66	57	50	⋮
400	T (ms)	2.5	3.75	5	6.25	7.5	8.75	10	⋮
	ω (rps)	400	267	200	160	133	114	100	⋮
Is the discharge suppressed?		✓	×	✓	×	✓	×	✓	⋮

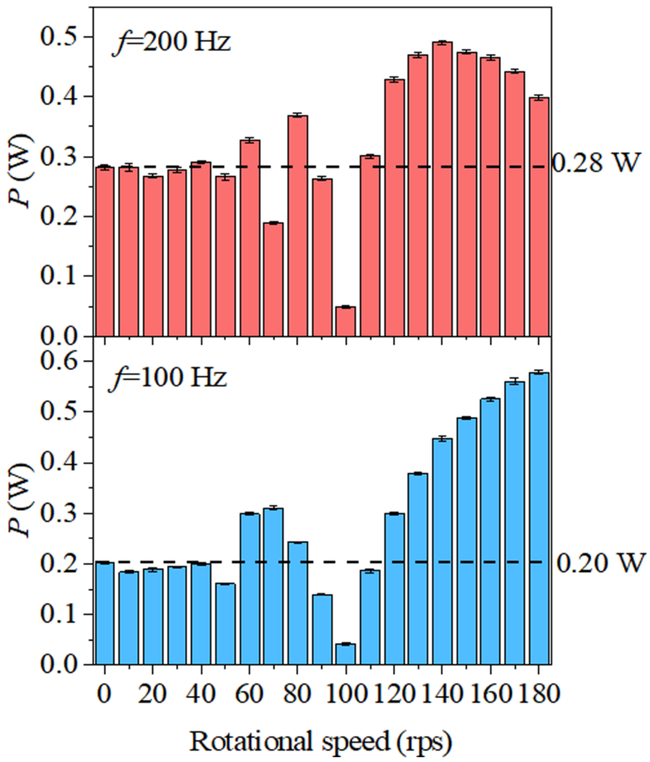

FIG. 9. Discharge powers at different speeds for the frequencies of 100 and 200 Hz at 10 kV.

different rotational speeds are taken and shown in Fig. 10(b). Results show that the discharge filaments can be observed at the second ground electrode when the rotational speed reaches 50 rps. In addition, the intensity of light at the second ground electrode becomes stronger as the velocity increases, indicating that more surface charges can move with the dielectric plate at higher velocities.

Studying the current pulses of discharge at the second ground electrode is a key point to gain further insight into the moving characteristics of surface charges. The currents through the second ground electrode at different rotating speeds are measured, and the single-shot current and voltage waveforms are presented in Fig. 11(a). It is worth pointing out that the voltage between the high-voltage electrode and the rotating dielectric plate is used to trigger the oscilloscope to ensure the consistency of the trigger time when acquiring current pulses through the second ground electrode. Thus, all voltage signals in Fig. 11 correspond to the voltage between the high voltage electrode and the rotating dielectric plate. To exclude random interference and increase the reliability of the experimental results, the current–voltage waveforms with the current accumulation of 130 times are shown in Fig. 11(b). It can be found that there are obvious negative current pulses for the rotating speed of 50 rps [Figs. 11(a_1) and 11(b_1)]. The negative current pulse corresponds to the discharge induced by the positive surface charges accumulated on the anodic needle half-cycle. Figure 11(b_1) shows that the time intervals corresponding to the appearance of the current pulses are not random but only fluctuate within a certain time. The time intervals are about 2.5 ms (one voltage cycle), indicating that those current pulses correspond to surface charges accumulated in two consecutive voltage cycles. Moreover, the number of current pulses tends to increase as the speed increases, which corresponds to the increase in light intensity

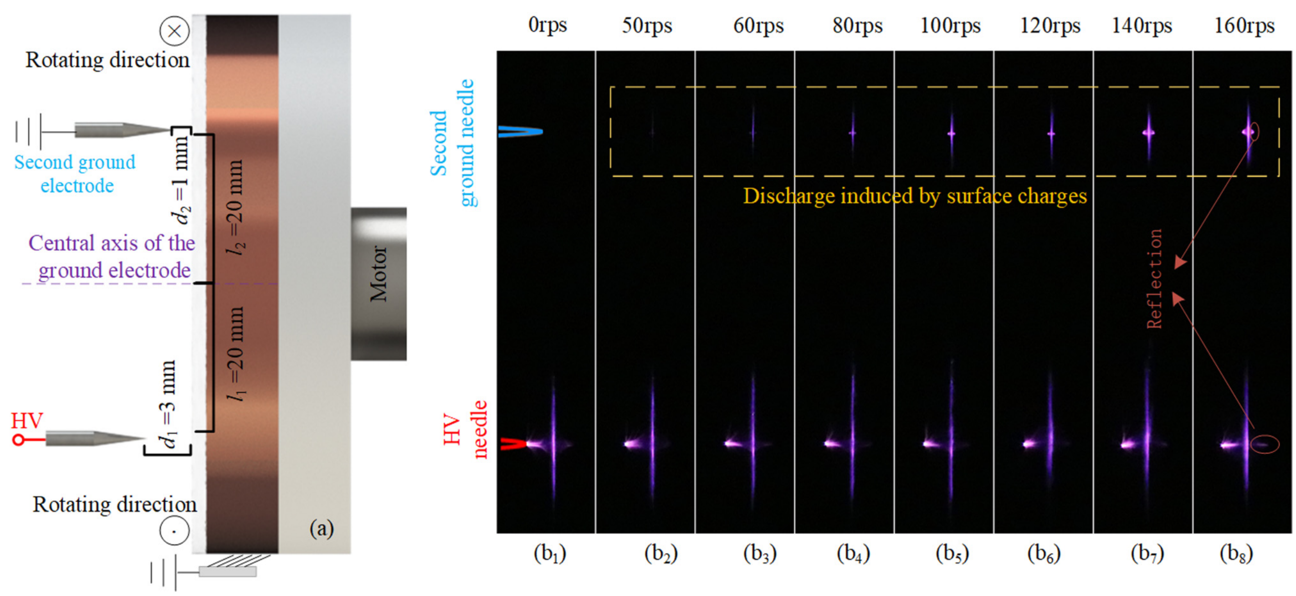

FIG. 10. (a) Diagram of the experimental setup with the introduction of the second ground electrode. (b) Discharge images with exposure time of 1/4 s at different rotational speeds.

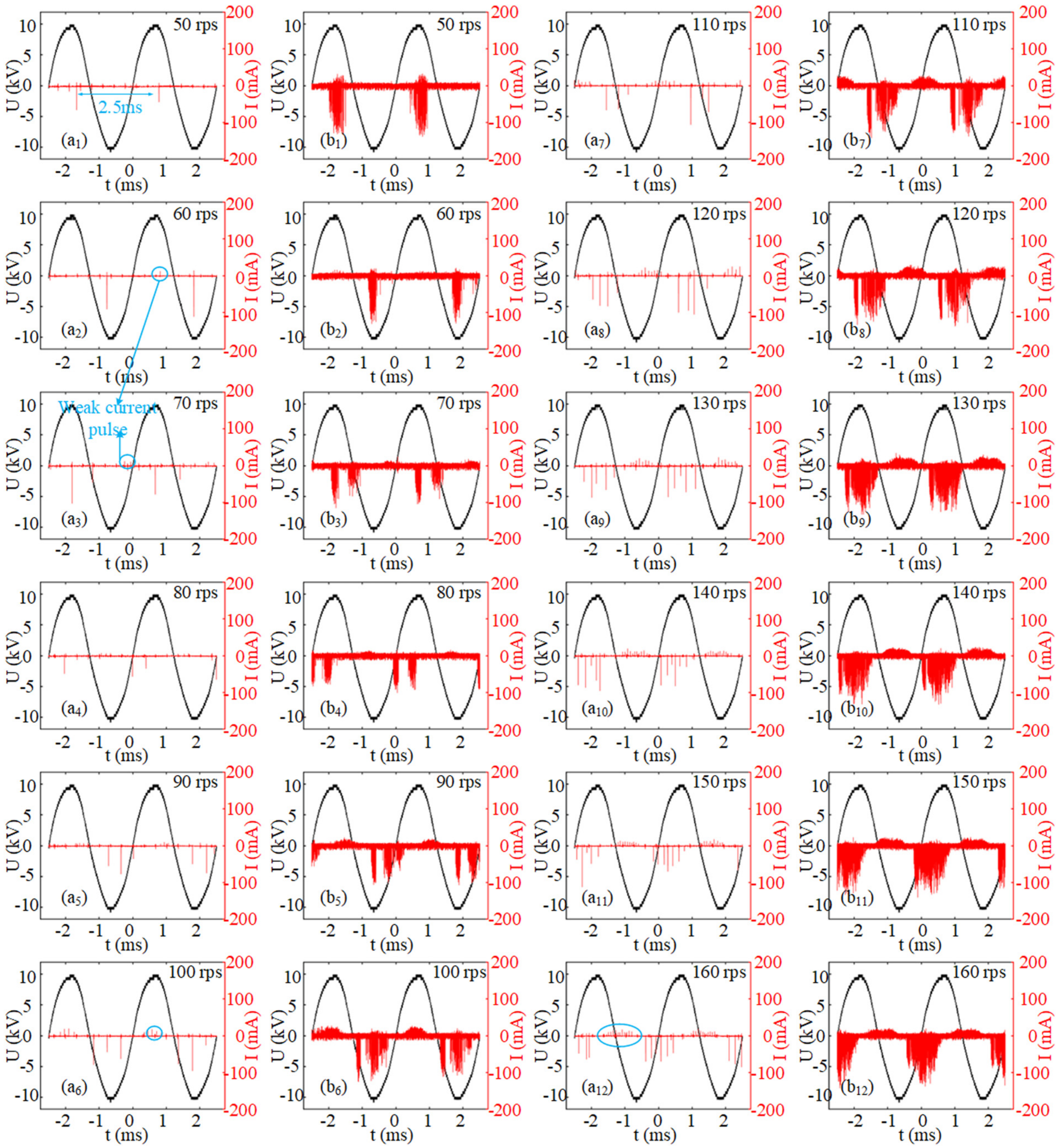

FIG. 11. (a_1)–(a_{12}) Single-shot current waveform of the second ground electrode at the rotational speeds from 50 to 160 rps, respectively. (b_1)–(b_{12}) Current waveform accumulated 130 times.

in Fig. 10(b). The positive weak current pulses can be found in Figs. 11(a_2)–11(a_{12}), which is induced by negative surface charges. The results indicate that the number of surface charges that can be efficiently transferred increases as the rotational speed increases.

In addition, the time corresponding to the current pulse with increasing rotational speeds is different, as shown in Figs. 11(b_1)–11(b_{12}), which is caused by the difference in the time spent on surface charges moving to the second ground electrode.

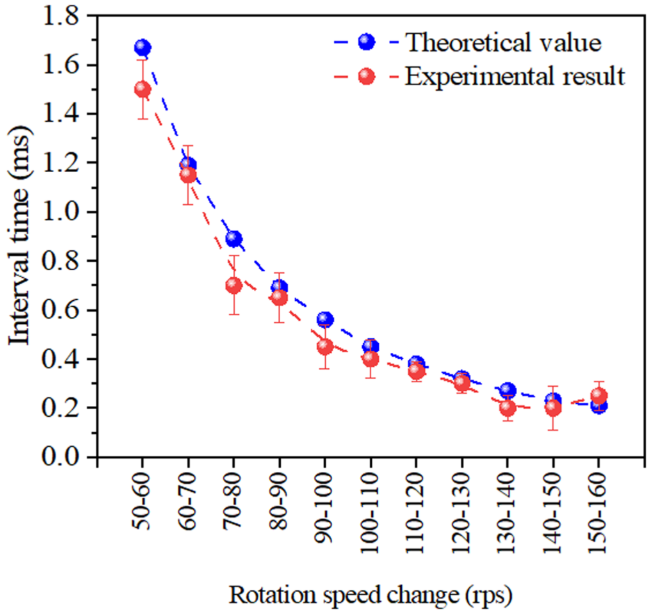

FIG. 12. Time intervals for the surface charges moving from the high voltage electrode to the second ground electrode when the speed is increased from ω to ω + 10.

The statistical time probability distribution is shown in Fig. S2 in the supplementary material. $\Delta t_{\omega_n-(\omega_n+10)}$ represents the time difference for the surface charge moving from the high voltage electrode to the second ground electrode when the speed is increased from ω to $\omega+10$. In theory, $\Delta t_{\omega_n-(\omega_n+10)}$ can be derived by the following method:

The time for the surface charges moving to the second ground electrode is

$$t = \frac{1}{2\omega}. \tag{5}$$

The time intervals at different rotational speeds can be calculated via

$$\Delta t = \frac{1}{2\omega_n} - \frac{1}{2\omega_m}, \tag{6}$$

where ω_n and ω_m represent different angular velocities of the dielectric plate.

For a speed increase of 10 rps, the time intervals can be given by

$$\Delta t_{\omega_n-(\omega_n+10)} = \frac{1}{2\omega_n} - \frac{1}{2(\omega_n+10)} = \frac{5}{\omega_n^2+10\omega_n}. \tag{7}$$

Experimental and theoretical time intervals for the rotational speeds from ω_n to (ω_n+10) are shown in Fig. 12. It can be found that the experimental results are in good agreement with theoretical derivation, which demonstrates that the surface charges can move with the dielectric at the same speed.

D. Numerical simulation and theoretical analysis of surface charges moving with a rotating dielectric plate on the plasma characteristics

Surface charges play an important role in the plasma characteristics in DBD.[37] Most of the surface charges can be considered laterally mobile on time-scales of 100s of ns after an electric breakdown, which result in that mostly flat charge distributions on the dielectric surface interspersed by Gaussian peaks at the locations of the volume discharge.[51] The surface charge region with Gaussian distribution plays the most critical role in the suppression of subsequent discharges in the same discharge cycle.[52] For stationary electrode DBD, these surface charges are always distributed on the dielectric surface below the needle tip. However, for the rotating dielectric plate DBD, those surface charges can move synchronously with the dielectric plate. Then, it is necessary to investigate the effect of the distribution for those surface charges on the reduced electric field. The numerical simulation of the effect of surface charge on the reduced electric field at the applied voltage of 10 kV is implemented and shown in Fig. 13, where the surface charge distribution range is set to 2 mm to reduce calculation costs, and the surface charge density is set to +10 nC/cm^2, which is close to that in the paper.[49,52–54] It can be found that both the reduced electric field (E_p) at the needle tip and the average reduced electric field (E_{ave}) for x = 5 mm in the air gap improve with the increasing distance (d_m) of surface charges, which indicates that the movement of surface charges is favorable to increase the electric field in the air gap, which is consistent with the result in Fig. 7.

To further investigate the mechanism of effective transfer of surface charges on the plasma enhancement at the same discharge cycle, Fig. 14(a) shows the moving distance (d_m) of surface charges at 200, 400, and 625 μs (quarter voltage cycle) for different rotational speeds, respectively. It can be found that d_m reaches 4, 8, and 12.6 mm for 160 rps at 200, 400, and 625 μs. This distance is enough to affect the total electric field in the gas gap. Figure 14(b) shows the mechanism of the effective transfer of surface charges to enhance the reduced electric field. For a stationary electrode, the surface charges always accumulate on the dielectric below the needle tip. The electric field (E_s) induced by the surface charge and the electric field (E_a) of the applied voltage are in opposite directions. The total electric field (E_t) in the discharge air gap is E_a–E_s, which indicates that E_s can result in the extinction of discharge when E_t is less than the breakdown threshold (E_b). For AC DBD, as E_a continues to increase, the streamer channel is re-ignited when E_t is greater than E_b. For the rotational dielectric plate, the distance from the needle tip to the central of surface charges distribution increases, as shown in Fig. 14(b$_2$). The electric field induced by surface charges (E_{sr}) is inversely proportional to the square of its distance from the needle tip. Hence, E_{sr} is less than E_s and the total electric field (E_{tr}) at the needle tip is larger than E_t, as shown in Figs. 14(b$_1$) and 14(b$_2$). Therefore, the rotation of the dielectric plate can enhance the E/N in DBD. The enhancement of the E/N is in favor of subsequent discharges at the same discharge cycle.

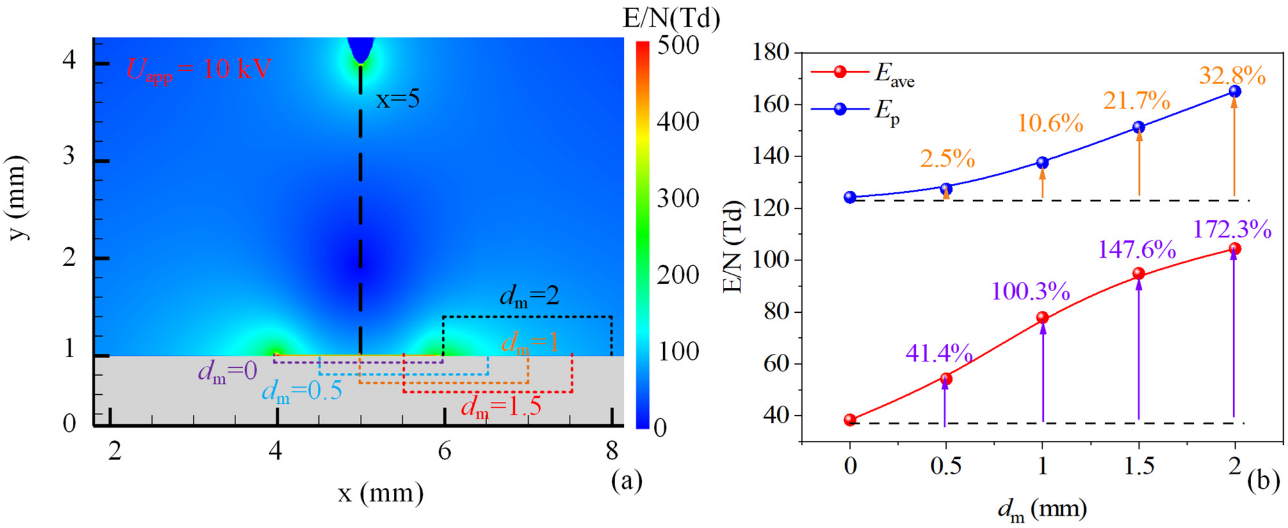

FIG. 13. Numerical simulation results of the effect of surface charge position on the electric field. (a) Electric field distribution when the applied voltage is 10 kV and the surface charge density is 10 nC/cm^2. (b) The magnitude of the electric field at the moving distance of surface charge. E_p is the reduced electric field at the needle tip and E_{ave} denotes the average reduced electric field in the gas gap at x = 5 mm.

Hence, rotating the dielectric plate can induce discharges on the falling edge of the voltage and increase the number of electrical breakdowns in Figs. 4 and 5. As the rotational speed decreases, d_m decreases, which leads to a weakening of the effect of increasing E_{tr} by rotating the dielectric plate. Based on the above conclusions, it can be concluded that the effective transfer of surface charges with rotating the dielectric plate can facilitate subsequent discharge generation by increasing the E/N in gas gap.

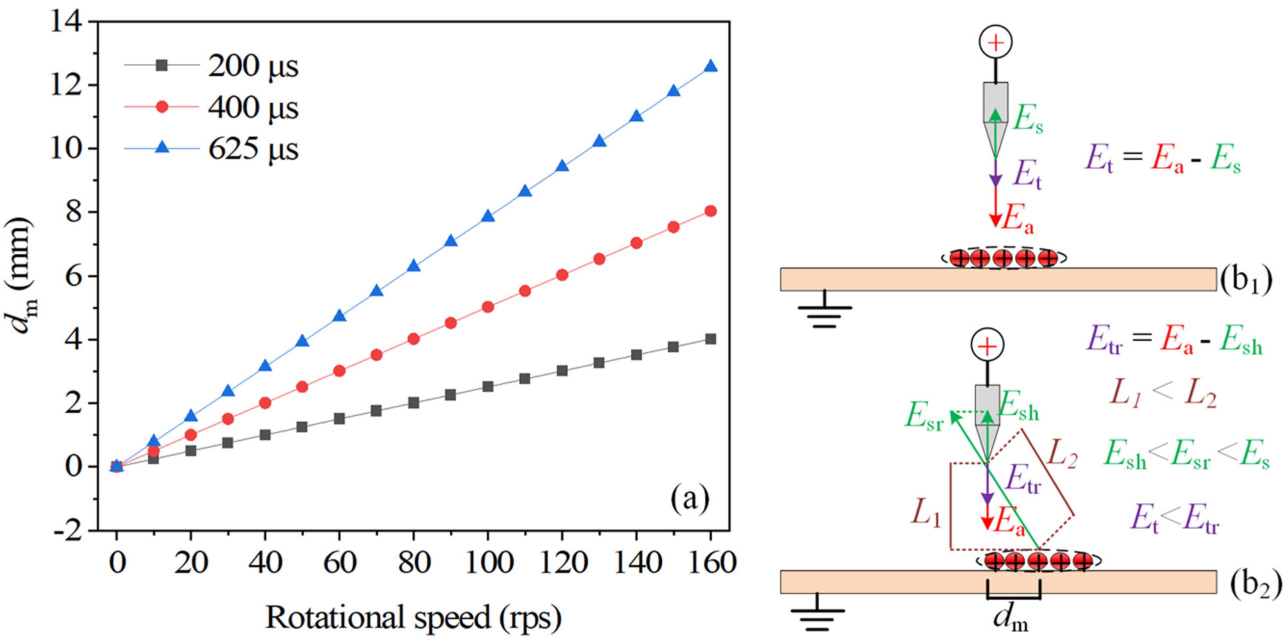

FIG. 14. (a) The moving distance (d_m) of the dielectric plate at different rotational speeds. (b) The effect of the surface charge movement on the electric field at the needle tip. (b$_1$) Stationary electrode. (b$_2$) Rotational dielectric plate. E_a denotes the electric field of applied voltage. E_s and E_{sr} are the electric fields induced by surface charges. E_{sh} is the component of E_{sr} along the vertical direction. E_t and E_{tr} represent the total electric fields at the tip of the needle along the vertical direction.

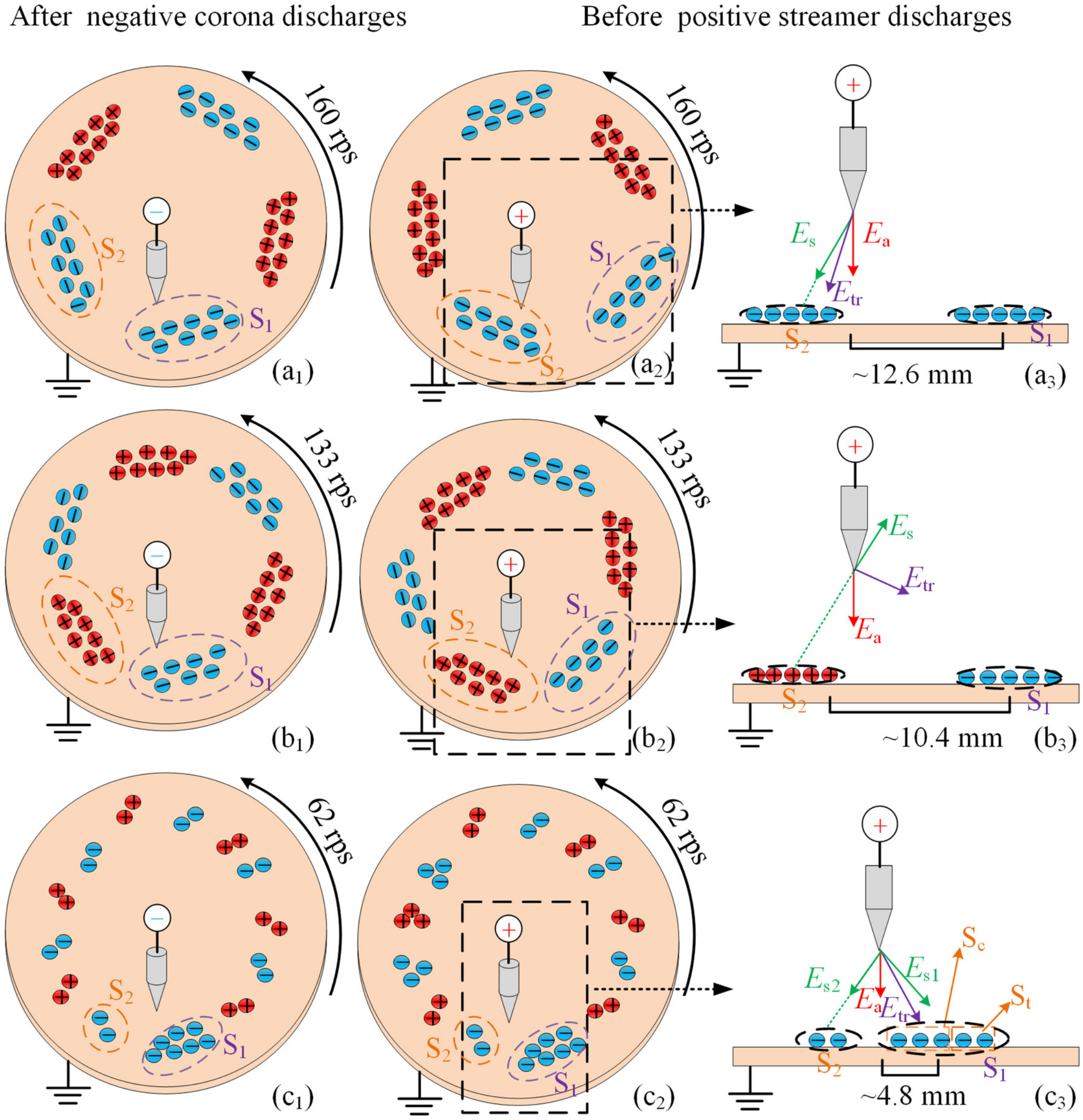

FIG. 15. Schematic diagram of surface charges affecting the direction of streamer bending. S_1 denotes the surface charges that have just accumulated on the dielectric and S_2 stands for the surface charges that have rotated one revolution. S_c is the surface charge that would be consumed by the subsequent positive streamer discharge and S_t denotes the surface charges that can transfer one revolution with the dielectric plate.

The effect of rotating the dielectric plate on streamer morphology is also caused by the movement of surface charges, and Fig. 15 shows the schematic diagram of surface charges affecting the streamer bending. It is worth pointing out that all the charges accumulated on the dielectric surface in a discharge cycle can influence the subsequent discharge and each clump of surface charges in Fig. 15 represents the cumulative result of all discharges in a discharge cycle. Therefore, the range of surface charge distribution depends on the rotating speed of the dielectric plate. Then, for the same rotating speed, the equal spreading diameter of positive and negative surface charges is assumed in Fig. 15. According to Table I, for 160 rps, the surface charge distribution after one negative half-cycle discharge is shown in Fig. 15(a$_1$). These surface charges can move with the rotating dielectric and the surface charges (S_1) move away from the discharge area. Assuming that the next streamer discharge will occur after a 1/4 voltage cycle, the travel distance is about 12.6 mm. Such a large distance suggests that they cannot affect the propagation of subsequent streamer after

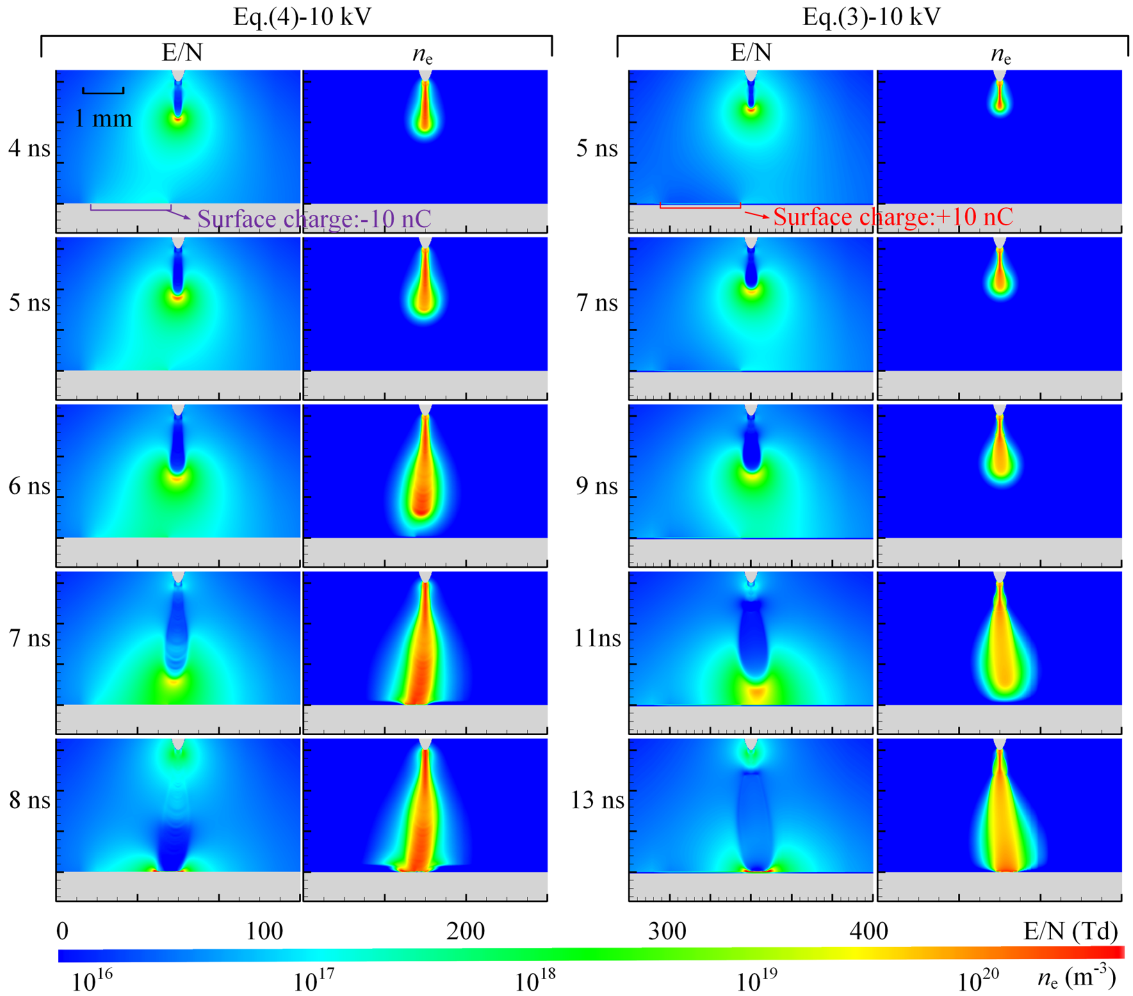

FIG. 16. Streamer propagation under pre-charging with different polarities.

voltage reversal. While the surface charges (S_2) approach the discharge area from the left side, they can induce the total electric field to bend to the left [Fig. 15(a$_3$)]. Therefore, the streamer is bent to the left direction at 160 rps in Fig. 3(l). For 133 rps, the effect of surface charges on streamer bending is similar to that of 160 rps. However, the total electric field bends to the right because that the direction of the electric field induced by surface charges and the applied electric field are the same, as shown in Fig. 15(b$_3$). According to Eq. (3), the effects of surface charges on streamer bending for 114 and 89 rps are the same as that for 160 rps, and the effects of the surface charge on streamer bending for 100 and 80 rps are the same as that for 133 rps. For 62 rps, the surface charge distribution after one negative half-cycle discharge is shown in Fig. 15(c$_1$). Before the next streamer discharge, the surface charges (S_1) move about 4.8 mm. The radius of the surface discharge distribution range is about 3.2 mm, as shown in Fig. 4(b$_4$). Some of the surface charges remain close to the needle tip, and they induce a bending of the streamer to the right. As a result, those surface charges can be consumed by the positive streamer discharge. Although some of the surface charges (S_t) far from the tip area can move with the dielectric plate, the number of surface charges is much smaller than that at high speed, which has been confirmed by the results in Figs. 10 and 11. Then, the surface charges (S_t) cannot dominate the direction of streamer bending. When the rotational speed reaches 80 rps, before the next streamer discharge, the surface charge (S_1) moves about 6.3 mm, which is approximately equal to the distribution range (diameter: 6.4 mm) of the surface discharge. Therefore, most of the surface charges are already far away from the area below the tip of the needle, and S_1 cannot dominate the direction of the streamer development. Therefore, the streamer bend at low speed (less than 80 rps) is dominated by charges accumulated in the immediately preceding half-cycle discharge, and the direction of the streamer channels depends on the rotation of the rotating dielectric plate. When the rotational speed is greater than or equal to 80 rps, the surface charge that rotates one revolution with the dielectric plate can dominate the bending of the streamer channels, and the direction of streamer channels depends on the matching of the rotating speed and applied voltage frequency, i.e., the morphology of streamers can be governed by Eqs. (3) and (4).

To further understand the matching mechanism of the rotating speed and the applied voltage frequency [Eqs. (3) and (4)], Fig. 16 shows the influence of surface charges with different polarities on streamer propagation. When Eq. (4) is satisfied, the negative surface charges enter the discharge region from the left side. In this case, the offset surface charges (x: from −2.75 to −4.75 mm; −10 nC/cm^2) are set on the dielectric surface, where the density of surface charges is close to that in the papers.[49,52–54] The simulation results show that the streamer channel (both the E/N and n_e) bends to the left, which is in good agreement with the experimental results for 89, 114, and 160 rps in Fig. 3. When Eq. (3) is fulfilled, the positive surface charges enter the discharge region from the left side. The simulation results show that both E/N and n_e bend to the right direction, which is consistent with the experimental results for 80, 100, and 133 rps in Fig. 3. Furthermore, it can be found that streamer propagation for Eq. (4) is faster than that for Eq. (3), which is attributed to the different effects of different polarities for surface charges on the discharge. The surface charges inhibit discharges when Eq. (3) is satisfied, while they promote discharges when Eq. (4) is fulfilled, which is consistent with the results in Table I. For high speeds (over 80 rps) when the direction of the electric field induced by the surface charges re-entering the discharge region is opposite to that of the applied voltage [Eq. (3) is satisfied], the bending direction of the streamer channel is consistent with that of the rotating dielectric plate. Furthermore, when the direction of the electric field induced by these surface charges re-entering the discharge region is the same as that of the applied voltage [Eq. (4) is fulfilled], the bending direction of the streamer channels is opposite to that of the rotating dielectric plate.

IV. CONCLUSIONS

In this paper, a needle-plate DBD device with a rotating dielectric plate has been proposed for improving plasma generation. The effects of the rotational dielectric plate on discharge power, streamer morphology, reduced electric field, and current pulses are investigated. The main results are as follows:

(1) The influence of the rotating dielectric plate on the discharge energy depends on the matching of the voltage frequency and the rotational speed. When $\omega = f_a/n$, the direction of the electric field induced by surface charges returning to the discharge area is consistent with that of the applied voltage; thus, the discharge power is suppressed. In contrast, the discharge power is increased as $\omega = f_a/(n - 0.5)$ due to that the direction of the electric field induced by surface charges is opposite to that of the applied voltage. In the latter case, both the number and the amplitude of the current pulses can be increased. For 400 Hz and 160 rps, the discharge power can be improved by 47% (from 0.45 W at 0 rps to 0.66 W at 160 rps). At the same conditions, the statistical results show that the amplitude and the number of current pulses are increased by 8.9% (from 56 to 61 mA) and 20% (from 10 to 12), respectively.

(2) Rotation of the dielectric plate can increase the spatial distribution of the streamer channels by inducing a bending of the streamer channels and an increase in the number of streamer branches. The results of OES and numerical simulations show that the transfer of surface charges can increase E/N, which facilitates the generation of subsequent discharges at the same discharge cycle. The movement of surface charges plays an important role in the bending direction of streamer channels. At low speed (less than 80 rps), the streamer bending is dominated by surface charges accumulated in the immediately preceding half-cycle discharge. In this case, the bending direction of the streamer channels is consistent with that of the rotating dielectric plate. When rotating speeds reach 80 rps, the bending of streamer channels is dominated by surface charges re-entering the discharge region. Then, the direction of streamer channels depends on the matching of rotating speed and applied voltage frequency.

(3) The electrical breakdown at the second ground electrode indicates that the surface charges move synchronously with the dielectric plate. The number of discharge current pulses at the second ground electrode increases with increasing rotation speeds, indicating that the surface charges can be transferred more efficiently at high rotational speeds.

SUPPLEMENTARY MATERIAL

See the supplementary material for detailed descriptions of the 2D fluid simulation model and the kinetic reactions, rate coefficients (Table S1), electromagnetic interference generated by the motor operation (Fig. S1), and the time probability distribution of the current pulses at the second ground electrode (Fig. S2).

ACKNOWLEDGMENTS

This work was supported by the National Natural Science Foundation of China (NNSFC) (Grant Nos. 52177130, 51877027, and 52107140) and the project funded by the China Postdoctoral Science Foundation (Nos. 2021M700662 and 2022T150083).

AUTHOR DECLARATIONS

Conflict of Interest

The authors have no conflicts to disclose.

Author Contributions

Guanglin Yu: Data curation (equal); Formal analysis (equal); Investigation (equal); Methodology (equal); Software (equal); Validation (equal); Writing – original draft (equal); Writing – review & editing (equal). **Nan Jiang:** Methodology (equal); Project administration (equal); Resources (equal); Validation (equal); Writing – review & editing (equal). **Bangfa Peng:** Formal analysis (equal); Funding acquisition (equal); Software (equal); Writing – review & editing (equal). **Haoyang Sun:** Data curation (equal); Formal analysis (equal). **Zhengyan Liu:** Formal analysis (equal); Validation (equal); Writing – review & editing (equal). **Jie Li:**

Conceptualization (equal); Formal analysis (equal); Funding acquisition (equal); Resources (equal); Supervision (equal).

DATA AVAILABILITY

The data that support the findings of this study are available within the article and its supplementary material.

REFERENCES

[1]U. Kogelschatz, "Ozone and beyond: The marvelous development of dielectric barrier discharges," J. Phys. D: Appl. Phys. **50**, 051001 (2017).
[2]N. Jiang, X. L. Lu, B. F. Peng, J. Li, K. F. Shang, N. Lu, and Y. Wu, "Physical and chemical properties of a magnetic-assisted DC superimposed nanosecond-pulsed streamer discharge plasma," J. Phys. D: Appl. Phys. **54**, 245203 (2021).
[3]R. Brandenburg, A. Bogaerts, W. Bongers, A. Fridman, G. Fridman, B. R. Locke, V. Miller, S. Reuter, M. Schiorlin, T. Verreycken, and K. Ostrikov, "White paper on the future of plasma science in environment, for gas conversion and agriculture," Plasma Process. Polym. **16**, 1700238 (2019).
[4]H. Gao, G. Wang, B. Chen, Y. Zhang, D. Liu, X. Lu, G. He, and K. Ostrikov, "Atmospheric-pressure non-equilibrium plasmas for effective abatement of pathogenic biological aerosols," Plasma Sources Sci. Technol. **30**, 053001 (2021).
[5]K. Liu, Q. Duan, Z. Zheng, R. Zhou, R. Zhou, W. Tang, P. Cullen, and K. Ostrikov, "Gas-phase peroxynitrite generation using dielectric barrier discharge at atmospheric pressure: A prospective sterilizer," Plasma Process. Polym. **18**, 2100016 (2021).
[6]A. Bogaerts, X. Tu, J. C. Whitehead, G. Centi, L. Lefferts, O. Guaitella, F. Azzolina-Jury, H. H. Kim, A. B. Murphy, W. F. Schneider, T. Nozaki, J. C. Hicks, A. Rousseau, F. Thevenet, A. Khacef, and M. Carreon, "The 2020 plasma catalysis roadmap," J. Phys. D: Appl. Phys. **53**, 443001 (2020).
[7]Y. Ma, Y. Wang, J. Harding, and X. Tu, "Plasma-enhanced N_2 fixation in a dielectric barrier discharge reactor: Effect of packing materials," Plasma Sources Sci. Technol. **30**, 105002 (2021).
[8]J. Zigon, M. Petric, and S. Dahle, "Dielectric barrier discharge (DBD) plasma pretreatment of lignocellulosic materials in air at atmospheric pressure for their improved wettability: A literature review," Holzforschung **72**, 979 (2018).
[9]Q. Z. Zhang, R. T. Nguyen-Smith, F. Beckfeld, Y. Liu, T. Mussenbrock, P. Awakowicz, and J. Schulze, "Computational study of simultaneous positive and negative streamer propagation in a twin surface dielectric barrier discharge via 2D PIC simulations," Plasma Sources Sci. Technol. **30**, 075017 (2021).
[10]B. Peng, K. Shang, Z. Liu, X. Yao, S. Liu, N. Jiang, N. Lu, J. Li, and Y. Wu, "Evolution of three-electrode pulsed surface dielectric barrier discharge: Primary streamer, transitional streamer and secondary reverse streamer," Plasma Sources Sci. Technol. **29**, 035018 (2020).
[11]N. R. Paw, T. Kimura, T. Ishijima, Y. Tanaka, Y. Nakano, Y. Uesugi, S. Sueyasu, S. Watanabe, and K. Nakamura, "Surface treatment of titanium dioxide nanopowder using rotary electrode dielectric barrier discharge reactor," Plasma Sci. Technol. **23**, 105505 (2021).
[12]D. Wang and T. Namihira, "Nanosecond pulsed streamer discharges: II.: Physics, discharge characterization and plasma processing," Plasma Sources Sci. Technol. **29**, 023001 (2020).
[13]Y.-R. Zhang, E. C. Neyts, and A. Bogaerts, "Enhancement of plasma generation in catalyst pores with different shapes," Plasma Sources Sci. Technol. **27**, 055008 (2018).
[14]D. Mei and X. Tu, "Conversion of CO_2 in a cylindrical dielectric barrier discharge reactor: Effects of plasma processing parameters and reactor design," J. CO_2 Util. **19**, 68 (2017).
[15]S. Li, X. Dang, X. Yu, G. Abbas, Q. Zhang, and L. Cao, "The application of dielectric barrier discharge non-thermal plasma in VOCs abatement: A review," Chem. Eng. J. **388**, 124275 (2020).
[16]H. Zhang, K. Li, T. Sun, J. Jia, X. Yang, Y. Shen, J. Wang, and Z. Lou, "The removal of styrene using a dielectric barrier discharge (DBD) reactor and the analysis of the by-products and intermediates," Res. Chem. Intermed. **39**, 1021 (2013).
[17]Y. Liu, S. A. Starostin, F. J. J. Peeters, M. C. M. van de Sanden, and H. W. de Vries, "Atmospheric- pressure diffuse dielectric barrier discharges in Ar/O_2 gas mixture using 200 kHz/13.56 MHz dual frequency excitation," J. Phys. D: Appl. Phys. **51**, 114002 (2018).
[18]Y. Liu, K. Van't Veer, F. J. J. Peeters, D. B. Mihailova, J. van Dijk, S. A. Starostin, M. C. M. van de Sanden, and H. W. de Vries, "Numerical simulation of atmospheric-pressure 200 kHz/13.56 MHz dual-frequency dielectric barrier discharges," Plasma Sources Sci. Technol. **27**, 105016 (2018).
[19]D. Z. Pai, D. A. Lacoste, and C. O. Laux, "Transitions between corona, glow, and spark regimes of nanosecond repetitively pulsed discharges in air at atmospheric pressure," J. Appl. Phys. **107**, 093303 (2010).
[20]Y. Zhang, L. Wei, X. Liang, and M. Šimek, "Ozone production in coaxial DBD using an amplitude-modulated AC power supply in air," Ozone Sci. Eng. **41**, 437 (2019).
[21]L. F. Dong, B. B. Liu, C. X. Li, and Y. Y. Pan, "Formation of kagome-white-eye-honeycomb hexagonal superlattice pattern in dielectric barrier discharge," Phys. Rev. E **100**, 063201 (2019).
[22]T. Li, H.-J. Yan, S.-Q. Yu, Y.-Y. Wang, J.-Q. Li, J. Song, and Q.-Z. Zhang, "Measurements of surface charge dynamics and surface-breakdown characteristics of surface dielectric barrier discharges," J. Appl. Phys. **132**, 153301 (2022).
[23]T. Somekawa, T. Shirafuji, O. Sakai, K. Tachibana, and K. Matsunaga, "Effects of self-erasing discharges on the uniformity of the dielectric barrier discharge," J. Phys. D: Appl. Phys. **38**, 1910 (2005).
[24]J. H. Choi, T. I. Lee, I. Han, B.-Y. Oh, M.-C. Jeong, J.-M. Myoung, H. K. Baik, K. M. Song, and Y. S. Lim, "Improvement of plasma uniformity using ZnO-coated dielectric barrier discharge in open air," Appl. Phys. Lett. **89**, 081501 (2006).
[25]K. Mitsuhashi, A. Komuro, K. Suzuki, C. Natsume, and A. Ando, "Spatiotemporal variations of the electrical potential on surface dielectric barrier discharges," Plasma Sources Sci. Technol. **30**, 04LT02 (2021).
[26]B. Peng, N. Jiang, X. Yao, Y. Ruan, D. Wang, K. Shang, N. Lu, T. Namihira, J. Li, and Y. Wu, "Experimental and numerical studies of primary and secondary streamers in a pulsed surface dielectric barrier discharge," J. Phys. D: Appl. Phys. **52**, 325202 (2019).
[27]R. Brandenburg, "Dielectric barrier discharges: Progress on plasma sources and on the understanding of regimes and single filaments," Plasma Sources Sci. Technol. **26**, 053001 (2017).
[28]M. Li, C. Li, H. Zhan, J. Xu, and X. Wang, "Effect of surface charge trapping on dielectric barrier discharge," Appl. Phys. Lett. **92**, 031503 (2008).
[29]Y. Tanakaran and K. Matra, "Influence of multi-pin anode arrangement on electric field distribution characteristics and Its application on microgreen seed treatment," Phys. Status Solidi A **218**, 2000240 (2021).
[30]N. Jiang, Y. Sun, B. Peng, J. Li, K. Shang, N. Lu, and Y. Wu, "Promoting volatile organic compounds removal by a magnetically assisted nanosecond pulsed gear-cylinder dielectric barrier discharge," Plasma Process. Polym. **19**, e2100108 (2022).
[31]P. Reichen, A. Sonnenfeld, and P. R. von Rohr, "Discharge expansion in barrier discharge arrangements at low applied voltages," Plasma Sources Sci. Technol. **20**, 055015 (2011).
[32]Y. F. Zhu, X. C. Chen, Y. Wu, J. B. Hao, X. G. Ma, P. F. Lu, and P. Tardiveau, "Simulation of ionization-wave discharges: A direct comparison between the fluid model and E-FISH measurements," Plasma Sources Sci. Technol. **30**, 075025 (2021).
[33]Y. Zhu, Y. Wu, B. Wei, H. Xu, H. Liang, M. Jia, H. Song, and Y. Li, "Nanosecond-pulsed dielectric barrier discharge-based plasma-assisted anti-icing: Modeling and mechanism analysis," J. Phys. D: Appl. Phys. **53**, 145205 (2020).
[34]X. Chen, Y. Zhu, Y. Wu, J. Hao, X. Ma, and P. Lu, "Modeling of fast ionization waves in pure nitrogen at moderate pressure," Plasma Sources Sci. Technol. **30**, 065002 (2021).

[35]Q.-Z. Zhang, L. Zhang, D.-Z. Yang, J. Schulze, Y.-N. Wang, and A. Bogaerts, "Positive and negative streamer propagation in volume dielectric barrier discharges with planar and porous electrodes," Plasma Process. Polym. **18**, 2000234 (2021).
[36]Y. Zhang, W. Ning, D. Dai, and Q. Wang, "Manipulating the discharge pulse number in an atmospheric helium dielectric barrier discharge with multiple current pulses per half cycle," Plasma Sources Sci. Technol. **28**, 104001 (2019).
[37]F. J. J. Peeters and M. C. M. Van De Sanden, "The influence of partial surface discharging on the electrical characterization of DBDs," Plasma Sources Sci. Technol. **24**, 015016 (2015).
[38]W. Z. Wang, T. Butterworth, and A. Bogaerts, "Plasma propagation in a single bead DBD reactor at different dielectric constants: Insights from fluid modelling," J. Phys. D: Appl. Phys. **54**, 214004 (2021).
[39]G. L. Yu, L. F. Dong, L. T. Guo, F. C. Liu, C. X. Li, Y. Y. Dou, C. H. Ren, and Y. Y. Pan, "Formation mechanism and application of a three-dimensional pattern in dielectric barrier discharge system," Phys. Plasmas **27**, 053503 (2020).
[40]S. Jahanbakhsh, V. Brüser, and R. Brandenburg, "Experimental investigation of single microdischarges in a barrier corona arrangement with a cathodic metal pin," Plasma Sources Sci. Technol. **29**, 015001 (2020).
[41]T. M. P. Briels, J. Kos, G. J. J. Winands, E. M. van Veldhuizen, and U. Ebert, "Positive and negative streamers in ambient air: Measuring diameter, velocity and dissipated energy," J. Phys. D: Appl. Phys. **41**, 234004 (2008).
[42]J. Qin and V. P. Pasko, "On the propagation of streamers in electrical discharges," J. Phys. D: Appl. Phys. **47**, 435202 (2014).
[43]Y.-Y. Wang, H.-J. Yan, H.-F. Guo, Y.-F. Xu, Q.-Z. Zhang, and J. Song, "Evolution of the uniformity in the repetitive unipolar nanosecond-pulse dielectric barrier discharge," Plasma Sources Sci. Technol. **30**, 075009 (2021).
[44]S. Wang, D.-Z. Yang, R. Zhou, R. Zhou, Z. Fang, W. Wang, and K. Ostrikov, "Mode transition and plasma characteristics of nanosecond pulse gas–liquid discharge: Effect of grounding configuration," Plasma Process. Polym. **17**, 1900146 (2020).
[45]P. Paris, M. Aints, F. Valk, T. Plank, A. Haljaste, K. V. Kozlov, and H. E. Wagner, "Intensity ratio of spectral bands of nitrogen as a measure of electric field strength in plasmas," J. Phys. D: Appl. Phys. **38**, 3894 (2005).
[46]J. H. Choi, T. I. Lee, I. Han, H. K. Baik, K. M. Song, Y. S. Lim, and E. S. Lee, "Investigation of the transition between glow and streamer discharges in atmospheric air," Plasma Sources Sci. Technol. **15**, 416 (2006).
[47]W. Yun, L. Yinghong, J. Min, S. Huimin, S. Changbing, and P. Yikang, "Experimental investigation into characteristics of plasma aerodynamic actuation generated by dielectric barrier discharge," Chin. J. Aeronaut. **23**, 39 (2010).
[48]L. Stollenwerk, S. Amiranashvili, J. P. Boeuf, and H. G. Purwins, "Measurement and 3D simulation of self-organized filaments in a barrier discharge," Phys. Rev. Lett. **96**, 255001 (2006).
[49]B. Zhang, J. Y. Xue, X. Y. Chen, S. L. Chen, H. B. Mu, Y. Xu, and G. J. Zhang, "Review of surface transient charge measurement on solid insulating materials via the Pockels technique," High Volt. **6**, 608 (2021).
[50]T. Li, H.-J. Yan, J.-Q. Li, J. Schulze, S.-Q. Yu, J. Song, and Q.-Z. Zhang, "The role of surface charge and its decay in surface dielectric barrier discharges," Plasma Sources Sci. Technol. **31**, 055016 (2022).
[51]F. J. J. Peeters, R. F. Rumphorst, and M. C. M. van de Sanden, "Dielectric barrier discharges revisited: The case for mobile surface charge," Plasma Sources Sci. Technol. **25**, 03LT03 (2016).
[52]R. Wild and L. Stollenwerk, "Phase-resolved measurement of the spatial surface charge distribution in a laterally patterned barrier discharge," New J. Phys. **16**, 113040 (2014).
[53]D. Tanaka, S. Matsuoka, A. Kumada, and K. Hidaka, "Two-dimensional potential and charge distributions of positive surface streamer," J. Phys. D: Appl. Phys. **42**, 075204 (2009).
[54]H. F. Guo, Y. Y. Wang, Y. F. Xu, Z. H. Fan, and C. S. Ren, "Comparative study on diffuse dielectric barrier discharges excited by unipolar positive versus bipolar pulses in atmospheric air," J. Appl. Phys. **125**, 163304 (2019).